Testing the assumptions underlying ocean mixing methodologies using direct numerical simulations

J.R. Taylor*

Department of Applied Mathematics and Theoretical Physics, University of Cambridge, Cambridge, CB3 0WA, U.K.

S.M. de Bruyn Kops

Department of Mechanical and Industrial Engineering, University of Massachusetts Amherst, Amherst, Massachusetts, USA 01003

C. P. Caulfield

BP Institute & Department of Applied Mathematics and Theoretical Physics University of Cambridge, Cambridge, CB3 0EZ, U.K.

P.F. Linden

Department of Applied Mathematics and Theoretical Physics, University of Cambridge, Cambridge, CB3 0WA, U.K.

Corresponding author address: John R. Taylor, CMS, DAMTP, University of Cambridge, Wilberforce Road, Cambridge, UK, CB3 0WA.

E-mail: J.R.Taylor@damtp.cam.ac.uk

ABSTRACT

Direct numerical simulations of stratified turbulence are used to test several fundamental assumptions involved in the Osborn, Osborn-Cox, and Thorpe methods commonly used to estimate the turbulent diffusivity from field measurements. The forced simulations in an idealized triply periodic computational domain exhibit characteristic features of stratified turbulence including intermittency and layer formation. When calculated using the volume-averaged dissipation rates from the simulations, the vertical diffusivities inferred from the Osborn and Osborn-Cox methods are within 40% of the value diagnosed using the volume-averaged buoyancy flux for all cases, while the Thorpe scale method performs similarly well in the simulation with a relatively large buoyancy Reynolds number ($Re_b \simeq 240$) but significantly overestimates the vertical diffusivity in simulations with $Re_b < 60$. The methods are also tested using a limited number of vertical profiles randomly selected from the computational volume. The Osborn, Osborn-Cox and Thorpe scale methods converge to their respective estimates based on volume-averaged statistics faster than the vertical diffusivity calculated directly from the buoyancy flux which is contaminated with reversible contributions from internal waves. When applied to a small number of vertical profiles, several assumptions underlying the Osborn and Osborn-Cox methods are not well-supported by the simulation data. However, the vertical diffusivity inferred from these methods compares reasonably well to the exact value from the simulations and outperforms the assumptions underlying these methods in terms of the relative error. Motivated by a recent theoretical development, it is speculated that the Osborn method might provide a reasonable approximation to the diffusivity associated with the *irreversible* buoyancy flux.

1. Introduction

Small-scale turbulence, defined here as three-dimensional overturning motions, plays an important role in setting the large-scale properties and circulation of the ocean. Turbulence influences the depth of the surface and bottom mixed layers by entraining stratified water into the mixed layer (e.g. Large et al. (1994); Pacanowski and Philander (1981)) thereby influencing biological productivity and the exchanges of heat and carbon between the atmosphere and ocean (Marra et al. 1990). On long timescales, turbulence gradually mixes distinct water masses in the ocean interior, thereby influencing the pathways of the global overturning circulation (Wunsch and Ferrari 2004; Marshall and Speer 2012).

Here we use the term 'mixing' to refer to the irreversible homogenization of a scalar quantity. This stands in contrast to 'stirring' which refers to the down-scale transfer of scalar variance and the generation of structures such as filaments by turbulent motions. Mixing relies on molecular diffusion of the scalar substance (e.g. heat or salt) which occurs at very small scales, while stirring is inevitably associated with larger scales. For a statistically homogeneous turbulent flow, mixing occurs at scales close to the Batchelor scale, $l_B = l_K/\sqrt{Pr}$ where $l_K = (\nu^3/\varepsilon)^{1/4}$ is the Kolmogorov scale, $Pr = \nu/\kappa_m$ is the Prandtl (or Schmidt) number, ν is the kinematic viscosity of the fluid, κ_m is the molecular scalar diffusivity, and ε is the dissipation rate of kinetic energy. For typical open ocean conditions where $\varepsilon \simeq 10^{-10} - 10^{-6}\mathrm{m}^2/\mathrm{s}^3$, the corresponding Kolmogorov scale is $l_K \simeq 1\mathrm{mm} - 1\mathrm{cm}$ and the thermal Batchelor scale is $l_B \simeq 0.3 - 3\mathrm{mm}$ while the haline Batchelor scale is an order of magnitude smaller. The very small scales involved make it difficult, if not impossible, currently to resolve scalar mixing in measurements or models.

Due to the difficulty associated with resolving the small scales involved in scalar mixing, observational methods generally involve calculating various proxies for mixing. A near-universal

assumption in the ocean mixing literature is that an ensemble of turbulent motions can be modelled through a turbulent diffusivity, defined as the ensemble-averaged scalar flux (in a particular coordinate direction) divided by the ensemble-averaged gradient (in an independently chosen direction). Although the turbulent diffusivity is a second rank tensor, our focus here will be on the vertical component, which we define as

$$\kappa \equiv \frac{-\langle w'c' \rangle}{\partial \langle c \rangle / \partial z}, \tag{1}$$

where w is the vertical velocity, c is a scalar quantity, angle brackets indicate an unspecified averaging operator assumed to be equivalent to ensemble-averaging, and primes denote departures from this average. Note that in some contexts (e.g. at fronts or in isopycnal coordinate ocean models) the diapycnal diffusivity might be more appropriate than the vertical diffusivity. In the simulations that will be analyzed here, the large-scale buoyancy gradient is aligned with the vertical direction, and hence the vertical and diapycnal diffusivities are equivalent by construction.

Indeed, estimating κ is one of the central aims of the ocean mixing community. Perhaps the most direct approach is to measure the vertical turbulent scalar flux $\langle w'c' \rangle$ through simultaneous measurements of the vertical velocity and scalar concentration. While this method is in principle possible (e.g. Moum (1996)), it can be extremely difficult to measure the vertical velocity accurately, and the correlation between the velocity and scalar concentration introduces another possible source of error. In addition, as we will see later, internal waves can induce a significant *reversible* contribution to the turbulent scalar flux and removing these contributions can be very difficult.

Other indirect methods of measuring the turbulent diffusivity necessarily rely on assumptions about the nature of small-scale turbulence. Indirect methods can be arranged in two categories: 'finescale' methods and 'microstructure' methods, each based around different assumptions. Sev-

eral finescale methods rely on the assumption that small-scale turbulence in the ocean interior is forced by the ambient internal wave field. These methods then link the mixing via small-scale turbulence with the properties of the internal wave field (e.g. Henyey et al. (1986); Gregg (1989a); Polzin et al. (1995); MacKinnon and Gregg (2003)).

Rather than relying on measurements of internal waves, microstructure methods use measurements of small-scale turbulence to infer the turbulent diffusivity. Two prominent microstructure methods are the Osborn-Cox method (Osborn and Cox 1972), which uses measurements of temperature or salinity variance and infers the scalar variance dissipation rate and diffusivity; and the Osborn method (Osborn 1980), which relates measurements of shear to the turbulent dissipation rate, and hence to the diffusivity. Gregg et al. (2018) provide a review and discussion of microstructure methods and their underlying assumptions.

An additional method for inferring the rate of mixing is the Thorpe-scale method. This method is perhaps best classified as intermediate between finescale and microstruture methods as it uses measurements of the scalar fields to infer the size of the largest turbulent motions. In this method unstable 'overturns' in a measured temperature, salinity, or density profile are first related to the dissipation rate and then to the turbulent diffusivity following the Osborn method (Osborn 1980). These methods and their underlying assumptions will be described in more detail in Section 3c below.

The primary objective of this paper is to evaluate microstructure and Thorpe-scale methods using output from direct numerical simulations (DNS) of forced stratified turbulence. By definition a DNS resolves *all* scales of turbulent motion. The simulations here have a molecular Prandtl number $Pr = 7$, a typical value corresponding to the diffusion of heat in seawater. Hence, the resolution of the simulations must be sufficient to capture scales near the Batchelor scale ($\sim$ 1mm in dimensional terms). Our aim is to simulate typical turbulent conditions in the ocean interior.

Even with a limited domain size, this makes the simulations extremely computationally expensive - here the simulations exceed 10^{12} gridpoints. The advantage of DNS is that turbulent quantities such as the dissipation rate and scalar flux can be evaluated exactly. This allows us to distinguish between uncertainties associated with measurement techniques from uncertainties associated with the underlying assumptions inherent in each method. Here, our focus is on such assumption-associated uncertainties.

The DNS that are analyzed here simulate turbulence in a relatively small $(\sim 5-10\text{m})$ three-dimensional domain. Periodic boundary conditions are applied to the velocity in all three directions, while a constant vertical background stratification is imposed. The computational domain can be interpreted as a small region embedded in the ocean interior. The simulations are forced by applying a scale-selective deterministic body force to the momentum equations to energize the large scales of the horizontal velocity. While the forcing term is intended to represent energy input from uncaptured large-scale motions, we do not attempt to simulate a particular internal wave spectrum at the large scales. We therefore do not attempt to test any finescale parameterizations and instead focus on microstructure and Thorpe-scale-based methods.

Many microstructure measurement techniques involve fitting a canonical spectrum to the measured spectrum obtained from a depth window (Gregg 1999) or spatially averaging over a prescribed depth interval (Moum et al. 1995) or an identified turbulent patch (Moum 1996). This effectively produces one value of dissipation or diffusivity for a given depth interval. Similarly, the Thorpe-scale method requires the calculation of the root-mean-square (*rms*) displacement scale with respect to a finite depth window. In section 3d we will apply the Osborn, Osborn-Cox, and Thorpe-scale methods to quantities calculated from vertical profiles extracted from the DNS, which generically can cover more than one 'patch' of turbulence in any single profile.

Turbulence in strongly stratified fluids is often highly intermittent in space and time (see e.g. Rorai et al. (2014); Portwood et al. (2016)). This raises the following question: how well can a limited set of observations reproduce the volumetrically-averaged turbulent diffusivity? In section 3d, we will also address this question by calculating the turbulent diffusivity with a limited number of vertical profiles extracted from the DNS. This can be interpreted as a best case scenario for observations of turbulent mixing without any measurement errors. In section 4, we discuss our results, and draw some conclusions.

2. Simulation setup and methodology

a. Governing Equations

The objective of the DNS is to simulate stratified turbulence in a quasi-equilibrated state where the energy input from large-scale forcing is balanced by small-scale dissipation and mixing. Periodic boundary conditions are applied in all three spatial directions, the details of which are given below. We do not directly consider the influence of any physical boundary and hence the computational domain can be viewed as a relatively small box embedded within the water column.

The simulations solve the non-hydrostatic Boussinesq equations that can be written in non-dimensional form normalized by a characteristic velocity scale, U, length scale, L, and background buoyancy frequency, N_0. The non-dimensional equations are

$$\nabla \cdot \mathbf{u} = 0 \tag{2a}$$

$$\frac{\partial \mathbf{u}}{\partial t} + \mathbf{u} \cdot \nabla \mathbf{u} = -\left(\frac{1}{\mathrm{Fr}}\right)^2 \rho \hat{\mathbf{z}} - \nabla p + \frac{1}{\mathrm{Re}} \nabla^2 \mathbf{u} + \mathscr{F} \tag{2b}$$

$$\frac{\partial b}{\partial t} + \mathbf{u} \cdot \nabla b + w = \frac{1}{\mathrm{Re}\,\mathrm{Pr}} \nabla^2 b \,, \tag{2c}$$

where the nondimensional parameters are a characteristic Froude number, the Prandtl number and a characteristic Reynolds number, defined as

$$\mathrm{Fr} \equiv \frac{U}{N_0 L}, \ \mathrm{Pr} \equiv \frac{\nu}{\kappa_m} \text{ and } \mathrm{Re} \equiv \frac{UL}{\nu}.$$

Note that the diffusion of the scalar is specified by a characteristic Péclet number $\mathrm{Pe} \equiv UL/\kappa_m = \mathrm{Re}\,\mathrm{Pr}$. The buoyancy, $b \equiv -g\rho/\rho_0$ can be related to temperature through a linear equation of state, $b = \alpha g(T - T_0)$ where ρ_0 and T_0 are reference density and temperature and α is the thermal expansion coefficient. The buoyancy b in Eq. 2c is defined as the departure from an imposed background gradient such that the total buoyancy is $b_T = b + N_0^2 z$. Periodic boundary conditions are then applied to b. In effect, this maintains a constant buoyancy difference between the top and bottom of the computational domain.

The periodic boundary conditions that are used here have implications for the flow that can develop. First, the relatively small domain size limits the scale of the motions that we are able to directly simulate. The body force ($\mathscr{F}$ in Eq. 2b) is meant to mimic the down-scale transfer of momentum and energy from motions that are larger than our computational domain, albeit in an idealized way. The periodic boundary conditions applied to the velocity and the departures from the background stratification imply that the local momentum and buoyancy flux at the top of the computational domain match the values at the bottom of the computational domain. However, these fluxes do not need to remain constant within the domain. As a result (and as we will see below), the simulations develop layers with relatively weak and strong stratification and the vertical shear associated with the horizontally-averaged velocity is non-zero.

b. Numerical methods

Equations (2) are solved in a triply periodic domain with the pseudospectral technique discussed in Almalkie and de Bruyn Kops (2012b). Spatial derivatives are computed in Fourier space, the nonlinear terms are computed in real space, and the solution is advanced in time in Fourier space with the variable-step, third-order, Adams-Bashforth algorithm with pressure projection. The nonlinear term in the momentum equation is computed in rotational form, and the advective term in the internal energy equation is computed in conservation and advective forms on alternate time steps. These techniques are standard to ensure conservation of energy and to eliminate most aliasing errors, but the simulations reported in this paper are fully de-aliased in accordance with the 2/3 rule via a spectral cutoff filter.

The body force $\mathscr{F}$ in (2) is implemented using the deterministic forcing schema denoted Rf in Rao and de Bruyn Kops (2011). The objective is to force all the simulations to have the same spectra $E_h(\kappa_h, \kappa_z)$ with $\kappa_h < \kappa_f$ and $\kappa_z = 0$. E_h is the power spectrum of the horizontal contribution to kinetic energy averaged over annuli of constant horizontal wave number κ_h and vertical wave number κ_z. The highest wave number forced is $\kappa_f = 16\pi/L_h$, with L_h the horizontal dimension of the numerical domain. Deterministic forcing requires choosing a target spectrum $E_f(\kappa_h < \kappa_f, 0)$. In contrast to turbulence that is isotropic and homogeneous in three dimensions, there are no theoretical model spectra for E_f (c.f. (Overholt and Pope 1998)). Therefore, run 2 from Lindborg (2006) was rerun using a stochastic forcing schema similar to that used by Lindborg and denoted schema Qg in Rao and de Bruyn Kops (2011). The spectrum for $E_h(\kappa_h < \kappa_f, 0)$ was computed from this simulation and used as the target for the simulations reported in the current paper.

In addition to forcing the large horizontal scales, 1% of the forcing energy is applied stochastically to the horizontal velocity components through wave number modes with $\kappa_h = 0$ and

$\kappa_z = 2\pi j/L_v$, $j = 2,3,4$. Here L_v is the vertical dimension of the numerical domain. This random forcing induces some vertical shear (Lindborg 2006). There is no forcing of the vertical velocity in the simulations.

The extent of the domain in the horizontal and vertical directions are L_h and L_v with L_h/L_v chosen to accommodate the vertical motions that develop in the flow. While the simulation domains are not cubes and the vertical extent of the domain varies with the chosen characteristic Froude number, the grid spacing Δ is the same in all directions. It is assumed for the purpose of choosing the resolution of the numerical grid that the flows are approximately isotropic at the smallest length scales in the simulation. Therefore, a three-dimensional grid with spacing $\Delta = L_h/N_x = L_h/N_y = L_v/N_z$ with N_x, N_y, and N_z being the number of grid points in the x, y, and z directions, respectively, is used and any small-scale anisotropy in the flows can be attributed to flow physics rather than to numerical artifacts of an anisotropic grid (c.f. Waite (2011)).

c. Parameters

Three simulations (labeled A, B and C) are analyzed here, and the related non-dimensional parameters are listed in Table 1. In each case the non-dimensional horizontal domain size is 2π. Simulations A and B have the same characteristic Froude number, $Fr = 0.0416$, representing relatively strong stratification. The Reynolds number is larger in Simulation A compared to Simulation B. Simulation C has a moderate Reynolds number and a larger characteristic Froude number representing weaker stratification.

Equations (2) are time-stepped until a statistically steady state is reached. The simulations can be described using non-dimensional parameters derived using turbulent properties in the final state. For this purpose it is useful to define the turbulent kinetic energy (TKE), $k \equiv \langle \mathbf{u}' \cdot \mathbf{u}' \rangle_V^{1/2}/2$, and

the TKE dissipation rate, $\langle \varepsilon \rangle_V \equiv 2\nu \left\langle s_{ij} s_{ij} \right\rangle_V$, where

$$s_{ij} \equiv \frac{1}{2}\left(\frac{\partial u_i'}{\partial x_j} + \frac{\partial u_j'}{\partial x_i} \right) \tag{3}$$

is the fluctuating rate of strain tensor, $\langle \cdot \rangle_V$ denotes an average over the full computational volume and primes denote departures from this volume average. The Reynolds number of the turbulent flow can then be characterized using the horizontal *rms* velocity, $u_{rms} \equiv \left\langle \mathbf{u}_h' \cdot \mathbf{u}_h' \right\rangle_V^{1/2}$ and a characteristic length scale. Two choices for the length scale are the integral length scale, L_h, and the turbulent length scale, $L_t \equiv \langle k \rangle_V^{3/2} / \langle \varepsilon \rangle_V$, thereby forming two derived Reynolds numbers,

$$Re_h \equiv \frac{u_{rms} L_h}{\nu}, \quad \text{and} \quad Re_t \equiv \frac{u_{rms} L_t}{\nu}. \tag{4}$$

Here L_h is computed from the longitudinal horizontal velocity spectra using the method of Comte-Bellot and Corrsin (1971) (see their Appendix E). Similarly, the relative strength of stratification can be quantified by two derived Froude numbers,

$$Fr_h \equiv \frac{u_{rms}}{N_0 L_h}, \quad \text{and} \quad Fr_t \equiv \frac{u_{rms}}{N_0 L_t}. \tag{5}$$

The integral scale L_h is a direct estimate of the length scale of the motions responsible for most of the kinetic energy in a flow. Since calculation of L_h requires two point statistics to compute, L_t has long been used as a surrogate, and we provide it here to facilitate comparisons with other data. For isotropic homogeneous turbulence, $\mathscr{D} \equiv L_h / L_t \approx 0.5$ (Pope 2000), and for decaying unstratified turbulence it has been observed to be as high as 1.81 (Sreenivasan 1998; Wang et al. 1996). For stratified turbulence with unity Pr, $\mathscr{D}$ ranges from 0.3 to 0.5 (de Bruyn Kops 2015; Maffioli and Davidson 2016) and decreases with decreasing buoyancy Reynolds number (defined in the next paragraph) (de Bruyn Kops and Riley 2019). In the current simulations with $Pr = 7$, $\mathscr{D}$ is approximately 0.1.

Stratification and viscosity can both act to inhibit turbulence motions. The combination of these effects can be quantified using a buoyancy Reynolds number (also referred to as a turbulent activity

coefficient Dillon and Caldwell (1980); Gibson (1980)),

$$Re_b \equiv \frac{\langle \varepsilon \rangle_V}{\nu N_0^2}. \tag{6}$$

From this definition, the buoyancy Reynolds number can be related to a ratio of Ozmidov and Kolmogorov scales, $Re_b = (L_O^V/L_K^V)^{4/3}$, where

$$L_K^V \equiv \left(\frac{\nu^3}{\langle \varepsilon \rangle_V} \right)^{1/4}, \quad \text{and} \quad L_O^V \equiv \frac{\langle \varepsilon \rangle_V^{1/2}}{N_0^{3/2}}. \tag{7}$$

Loosely, the Ozmidov scale characterizes the size of the largest turbulent overturns permitted by stratification and the Kolmogorov scale characterizes the size of the smallest motions permitted by viscosity. Therefore, Re_b provides a measure of the dynamic range associated with turbulent overturning motions, largely unaffected by either buoyancy or viscosity. The simulations in Table 1 are listed in order of increasing Re_b. Values of Re_b in this range are common in the ocean interior according to a recent estimate based on ARGO data (Salehipour et al. 2016) and fine-scale parameterizations (Gregg 1989b). Larger values of Re_b are also observed (Moum 1996), but these are not currently accessible with DNS of strongly stratified flows with realistic Pr.

For comparison with observations it is useful to construct a set of dimensional parameters for each simulation. Here, this is done by setting the dimensional vertical domain size to 5m and the kinematic viscosity to $10^{-6}\mathrm{m}^2\mathrm{s}^{-1}$, appropriate for water. The dimensional domain size was chosen to match roughly the size of typical turbulent patches in the ocean interior and the vertical size typically used for averaging microstructure measurements (Moum 1996; Smyth et al. 2001). The horizontal dimensional domain size is 40m in Simulations A and B and 10m in Simulation C. As we will see, the domain size is sufficient to accommodate many turbulent overturns. For comparison the largest dimensional domain size used in the simulations of Smyth et al. (2001) (for $Pr = 7$) was $2.73 \times 1.36 \times 0.34$m.

Once the dimensional domain size and kinematic viscosity are set, the dimensional time scale can be found from the characteristic Reynolds number, Re. Some of the dimensional parameters are listed in Table 2. The dimensional values of the background buoyancy frequency, N_0, are in the range $3.7 \times 10^{-3}\mathrm{s}^{-1}$ to $1.4 \times 10^{-2}\mathrm{s}^{-1}$, corresponding to buoyancy periods ranging from 28.0 to 7.4 min. The weakest stratification considered here is within the range observed by Moum (1996) in the main thermocline while the strongest stratification considered here is more typical of the seasonal pycnocline (e.g. Alford and Pinkel (2000b)). The dimensional average turbulent dissipation rate spans more than two orders of magnitude and contains values typically measured in the ocean interior (e.g. Moum (1996); Gregg (1989b)). The vertical turbulent diffusivity calculated with the volume-averaged horizontal buoyancy flux, $\kappa_d^V \equiv -\langle B \rangle_V / \langle N^2 \rangle_V$ ranges from $2.2 \times 10^{-6}\mathrm{m}^2\mathrm{s}^{-1}$ in Simulation A to $7.2 \times 10^{-5}\mathrm{m}^2\mathrm{s}^{-1}$ in Simulation C. The very small diffusivity in Simulation A is consistent with the observation by Ivey and Imberger (1991) that turbulence collapses for $Re_b \lesssim 15$. However, as discussed by Rorai et al. (2014); Portwood et al. (2016), strongly stratified turbulence is highly intermittent in space and time and (as we will see below) the volume-averaged statistics are not indicative of the turbulence at single points in space.

3. Results

a. Vertical section and profiles

Turbulence and mixing are intermittent across a wide range of scales in the DNS. On small scales, the statistics of energy and buoyancy variance dissipation are skewed with a small number of large events dominating the volume average. This is a well-known property of high Reynolds number turbulence in unstratified flows (Sreenivasan and Antonia 1997) and intermittency in scalar mixing is discussed extensively in Warhaft (2000). On larger scales, turbulence occurs in localized

bursts separated by relatively quiescent flow. Similar behavior has been observed in numerous previous studies (e.g. Riley and de Bruyn Kops (2003); Hebert and de Bruyn Kops (2006a); Rorai et al. (2014); Portwood et al. (2016)).

The top row in Figure 1 shows a vertical cross-section of buoyancy, b, and the TKE dissipation rate, ε, from Simulation C. The other simulations (not shown) have qualitatively similar features. A series of distinct layers are visible in the buoyancy field with relatively thick weakly stratified regions separated by relatively thin and more strongly stratified interfaces. The turbulent dissipation rate exhibits localized patches of strong turbulence similar to those described in Portwood et al. (2016). Maximum local values of ε are up to 30 times larger than the volume average.

The lower panels in Figure 1 show a close-up view of the flow in the boxed regions labeled 1, 2, and 3 in the top panels. In order to quantify mixing in each region, it is convenient to introduce the perturbation potential energy. In a volume with constant background buoyancy gradient N_0^2, the perturbation potential energy is $\left\langle b'^2 \right\rangle_V / (2N_0^2)$ and its associated dissipation rate can be written as

$$\chi \equiv \frac{\kappa_m \nabla b' \cdot \nabla b'}{N_0^2}. \tag{8}$$

Since N_0^2 is constant in our simulations, χ is proportional to the dissipation rate of buoyancy variance, and hence is a natural measure of irreversible mixing (see Salehipour and Peltier (2015) for a detailed discussion).

Region 1 is associated with relatively large kinetic and potential energy dissipation rates. As seen in the buoyancy field, in the middle of this region is a ~ 0.5 m vertical overturn. At the center of the overturn χ is relatively weak while ε remains large. Along the edges of the overturn χ and ε are of similar magnitude. In other words, mixing is more efficient on the flanks of the overturn than in the center of the overturn.

Region 2 exhibits a moderate value of ε and an undulating density interface passes through the region. While ε is relatively uniform in the region, χ is significantly larger near the density interface than in the mixed regions above and below the interface. Small overturns, 5-10 cm in height, appear along the density interface, but these features appear irregular.

Region 3 is characterized by relatively small values of ε and a relatively flat density interface. A vertically-sheared flow exists on either side of the density interface (not shown) and a series of what appear to be shear-induced billows can be seen. These billow-like structures are highlighted by relatively large values of χ.

Statistics collected along a single vertical profile corresponding to the white dashed line in Figure 1 are shown in Figure 2. The red dashed line in Figure 2(a) shows the 1D sorted buoyancy profile. The displacement scale L_d is the change in height of a fluid parcel from its unsorted to sorted positions. Several features in the profiles shown in Figure 2 resemble qualitatively the observed profiles reported in Moum (1996) such as the step-like structure in the density field and the corresponding structure in the Thorpe displacement scale (see, e.g. Figure 1b in Moum (1996)). The buoyancy flux, $w'b'$, alternates in sign along the vertical profile, indicating reversible transfer between perturbation potential and kinetic energy.

The kinetic and potential energy dissipation rates are highly intermittent (see panels d and 3 in Figure 2). There is no clear correlation between locations with large ε and χ. As a result, a local mixing efficiency, $\eta(\mathbf{x},t)$, which may be defined as

$$\eta(\mathbf{x},t) \equiv \frac{\chi}{\chi+\varepsilon}, \tag{9}$$

fluctuates rapidly between 0 and 1 (Figure 2f).

b. Length scales

The relative importance of stratification and viscosity to the turbulent motions at a particular scale can be quantified by comparing various length scales associated with stratified turbulence (Smyth and Moum 2000). Figure 3 shows characteristic length scales for each simulation, plotted as a function of the buoyancy Reynolds number, Re_b. Here, dimensional values are plotted, where the vertical domain size is set to 5m as discussed above.

In dimensional terms, the Kolmogorov scale, L_K, ranges from 2.4mm to 8.7mm, while the Batchelor scale, $L_B = L_K/\sqrt{Pr}$ ranges from 0.9mm to 3.3mm. The isotropic grid spacing, $\Delta_{x,y,z}$ is always less than twice the Batchelor scale, ensuring that the DNS is sufficiently well-resolved. The wide scale separation between the domain size and the grid spacing gives an indication of the large computational cost of these simulations.

There are several different ways to construct a Thorpe scale from a three-dimensional dataset (see Smyth and Moum (2000) and Mashayek et al. (2017a) for further discussion). For example, it would be possible to sort a three-dimensional density field (e.g. Winters and D'Asaro (1996)) and calculate the Thorpe scale from the *rms* vertical displacements with respect to the volumetrically-sorted profile. Here, motivated by oceanographic observations where three-dimensional sorting is typically not possible, we instead vertically sort the density profile at each horizontal gridpoint. The Thorpe scale is then calculated from each vertical profile and the result shown in Figure 3 is averaged over all horizontal gridpoints. Specifically,

$$L_T^V \equiv \left\langle \left\langle L_d^2 \right\rangle_z^{1/2} \right\rangle_{x,y}, \tag{10}$$

where $\langle\cdot\rangle_z$ denotes an average in the vertical direction and $\langle\cdot\rangle_{x,y}$ denotes an average in the horizontal directions. Later, in section 3d, we will examine the sensitivity of the Thorpe scale estimates calculated with a limited number of vertical profiles.

The dimensional Thorpe and Ozmidov scales calculated using volumetric simulation data, L_T^V and L_O^V are both $\simeq 10$ cm and increase somewhat with increasing buoyancy Reynolds number. The Ozmidov scale increases with Re_b faster than the Thorpe scale such that the ratio L_O^V/L_T^V is 0.53 in simulation A, 0.56 in simulation B, and 0.92 in simulation C. This can be compared with $L_O/L_T \simeq 0.8$ suggested by Dillon and Caldwell (1980). The dependence of this ratio on the flow parameters is consistent with the recent conclusions of Mater et al. (2015) and Scotti (2015).

c. Testing of Osborn, Osborn-Cox, and Dillon methods

In this section, we will compare the vertical turbulent diffusivity diagnosed directly from the simulations with values inferred from the Osborn, Osborn-Cox, and Dillon methods. Before giving the results, a brief description of each method is given below, highlighting in particular some of the key assumptions behind each method.

1) OSBORN-COX METHOD

Starting from an equation for entropy density, Osborn and Cox (1972) derived a method to estimate the vertical turbulent diffusivity from measurements of microscale temperature or conductivity. Here, we will write the equations in terms of buoyancy b with the understanding that this is more closely related to temperature than salinity since the Prandtl number is 7 in the DNS. The buoyancy variance budget (as noted above this is linearly related to the perturbation potential energy in this context) can be written as

$$\left(\frac{\partial}{\partial t} + \langle \mathbf{u} \rangle \cdot \nabla\right) \left\langle b'^2 \right\rangle + \nabla \cdot \left(\left\langle \mathbf{u}' b'^2 \right\rangle - \kappa_m \nabla \left\langle b'^2 \right\rangle \right) = -2 \left\langle \mathbf{u}' b' \right\rangle \cdot \nabla \langle b \rangle - 2\kappa_m \left\langle \nabla b' \cdot \nabla b' \right\rangle, \quad (11)$$

where angle brackets denote an average over some arbitrary volume (e.g. Pope (2000)). Assuming that terms on the left hand side, the time rate of change and flux divergence, are both small, Eq. 11

reduces to a production-dissipation balance

$$-\left\langle \mathbf{u}'b'\right\rangle \cdot \nabla \left\langle b\right\rangle = \kappa_m \left\langle \nabla b' \cdot \nabla b'\right\rangle = \left\langle \chi\right\rangle \left\langle N^2\right\rangle, \tag{12}$$

using Eq. 8. Further neglecting the horizontal buoyancy flux and defining the vertical diffusivity in terms of these (arbitrary) volume average, i.e. $\kappa \equiv -\left\langle B\right\rangle / \left\langle N^2\right\rangle$ yields an estimate of the vertical turbulent diffusivity,

$$\kappa_{O-C} \equiv \frac{-\left\langle B\right\rangle}{\left\langle N^2\right\rangle} \simeq \frac{\left\langle \chi\right\rangle}{\left\langle N^2\right\rangle}. \tag{13}$$

2) Osborn method

The Osborn method (Osborn 1980) provides a way to estimate the vertical diffusivity associated with small-scale turbulence from the TKE dissipation rate. In deriving the method, Osborn made several key assumptions (see e.g. Mashayek et al. (2013) for further discussion), including that the vertical diffusivity is dominated by fully developed turbulence, and that the turbulence exhibits a quasi-steady balance between production, dissipation and diapycnal mixing *when suitably averaged* so that the mixing can be related to the dissipation rate. Therefore, the TKE budget reduces to a balance between production, buoyancy flux, and dissipation, (with crucially no contribution from advective or boundary processes) i.e.

$$\left\langle P\right\rangle = \left\langle \varepsilon\right\rangle - \left\langle B\right\rangle, \tag{14}$$

where

$$\left\langle P\right\rangle \equiv -\left\langle u_i' u_j'\right\rangle \frac{\partial \left\langle u_i\right\rangle}{\partial x_j} \tag{15}$$

is the turbulent shear production. Osborn (1980) further assumed that small-scale turbulence is isotropic so that the dissipation rate can be determined from just one component of the deformation rate tensor. We do not test this assumption here and instead evaluate the production and

dissipation using the full deformation rate tensor. The appropriateness of the assumption of small-scale isotropy for stratified turbulence has been discussed extensively in recent papers (e.g. Hebert and de Bruyn Kops (2006b); Almalkie and de Bruyn Kops (2012a); de Bruyn Kops (2015)). Osborn (1980) further suggested that the assumption of quasi-steadiness and hence the averaging operator could be applied to vertical profiles through turbulent patches ranging from 1-10 m in size.

Using the classical definition of the flux Richardson number, $R_f \equiv -\langle B \rangle / \langle P \rangle$ (or $R_f = \langle B \rangle / (\langle B \rangle - \langle \varepsilon \rangle)$ using Eq. 14) the buoyancy flux may be expressed in terms of the TKE dissipation rate ε as

$$\langle B \rangle = -\left(\frac{R_f}{1 - R_f} \right) \langle \varepsilon \rangle . \tag{16}$$

Then, the vertical turbulent diffusivity, $\kappa = -\langle B \rangle / \langle N^2 \rangle$, can be related to ε to yield the estimate

$$\kappa_O = \Gamma \frac{\langle \varepsilon \rangle}{\langle N^2 \rangle}, \tag{17}$$

where $\Gamma \equiv \left(\frac{R_f}{1 - R_f} \right)$. The turbulent flux coefficient Γ is often referred to as a 'mixing efficiency', although in principle it can be greater than one, and there has been much recent activity attempting to produce appropriate parameterizations for this quantity in terms of various flow parameters, see for example Salehipour et al. (2016); Mashayek et al. (2017b); Monismith et al. (2018).

3) THORPE-SCALE METHOD

Thorpe (1977) proposed a method to estimate the averaged dissipation rate based on vertical profiles of potential density. An advantage of this method is that it can be applied to more readily available data (Gargett and Garner 2008). To calculate the Thorpe scale, a density profile is first sorted so that the sorted density is a monotonic function of height. The displacement length L_d is the difference in height of a water parcel from its unsorted to sorted location (figure 2(c)). The

Thorpe scale is then calculated by taking the root mean square of L_d, i.e.

$$L_T^P = \left\langle L_d^2 \right\rangle_P^{1/2}, \tag{18}$$

where angle brackets are typically taken to represent an appropriate 'patch' average, for example taken over a single overturning turbulent patch or an ensemble of such patches obtained from vertical profiling instruments (Thorpe 2005). Thorpe (1977) conjectured that L_T^P may be linearly related to the Ozmidov scale calculated with patch-averaged quantities, $L_O^P = \langle \varepsilon \rangle_P^{1/2} \left\langle N^2 \right\rangle_P^{-3/2}$. This then gives an estimate of the dissipation rate

$$\langle \varepsilon \rangle_P = R_{OT}^2 \left(L_T^P \right)^2 \left\langle N^2 \right\rangle_P^{3/2}, \tag{19}$$

where the coefficient of proportionality, $L_O^P / L_T^P \equiv R_{OT} \simeq 0.8$, is based on observations by Dillon and Caldwell (1980), although there is mounting evidence that estimates of this coefficient can be both biased and uncertain (Mater et al. 2015; Scotti 2015; Mashayek et al. 2017a). Then, using Eq. 17 yields an estimate for the vertical turbulent diffusivity,

$$\kappa_T = 0.64 \Gamma \left(L_T^P \right)^2 \left\langle N^2 \right\rangle_P^{1/2}. \tag{20}$$

4) Comparison

The underlying assumptions behind the three methods described above are questionable in strongly stratified flows where turbulent events are highly intermittent in time and space as illustrated in Figure 1. This concern becomes stronger when a small subset of the flow is sampled, for example using a small number of vertical profiles, since the various averages being taken become less reliable as representative of turbulent mixing events within the flow. Before addressing the issue of incomplete sampling and averaging, we will first examine the performance of the approximate methods described above, compared with the 'direct' calculation of κ formed using the

volume-averaged buoyancy flux and stratification, i.e.

$$\kappa_d^V = \frac{-\langle B \rangle_V}{\langle N^2 \rangle_V}. \tag{21}$$

When calculated using data from the full computational volume, the vertical turbulent diffusivity associated with the Osborn-Cox, Osborn, and Thorpe methods can be written

$$\kappa_{O-C}^V = \frac{\langle \chi \rangle_V}{\langle N^2 \rangle_V}, \quad \kappa_O^V = \Gamma \frac{\langle \varepsilon \rangle_V}{\langle N^2 \rangle_V}, \quad \kappa_T^V = 0.64\Gamma \left(L_T^V\right)^2 \langle N^2 \rangle_V^{1/2}, \tag{22}$$

respectively, where $\langle \cdot \rangle_V$ denotes an average over the full computational volume and L_T^V is defined in Eq. 10. Figure 4 shows κ_{O-C}^V, κ_O^V and κ_T^V, normalized by κ_d^V as defined in Eq. 21 and plotted against the buoyancy Reynolds number to differentiate the three simulations. The dimensional values of κ_d^V are $2.2 \times 10^{-6} \mathrm{m^2 s^{-1}}$ in Simulation A, $1.8 \times 10^{-5} \mathrm{m^2 s^{-1}}$ in Simulation B, and $7.2 \times 10^{-5} \mathrm{m^2 s^{-1}}$ in Simulation C, roughly spanning typical values found in the ocean interior (Waterhouse et al. 2014).

Even with perfect sampling of the 3D volume, there are significant differences between the various estimates of κ. The estimates using the Osborn and Osborn-Cox methods, κ_O^V and κ_{O-C}^V are within 40% of κ_d^V, and there is no clear trend with Re_b. The Thorpe-scale method underestimates κ_d^V by about 50% in Simulation C, but significantly overestimates κ_d^V in Simulations A and B. Recall that our simulations are analyzed at a statistically steady state. It is possible that temporal variability could lead to larger biases when these methods are applied to oceanographic data. In addition, when the Thorpe scale is small and/or when the density contrast is weak, it can be difficult to distinguish between real overturns and measurement error associated with a CTD profile (Ferron et al. 1998; Alford and Pinkel 2000a; Johnson and Garrett 2004).

d. Vertical profile-averaged statistics

The estimates of the vertical turbulent diffusivity described above were calculated using simulation data extracted from the full three-dimensional volume. In contrast, data collected from the ocean are necessarily much more limited. In this section, we explore the sensitivity of the estimates of κ when calculated with limited data. Note that we do not consider instrument error or biases introduced when converting measured quantities into physical quantities like the dissipation rate. Instead, we assume that the simulated field can be sampled perfectly at discrete points in space and focus on the influence of limited data availability.

The most common sampling strategy to infer κ is to collect velocity, temperature and/or conductivity along roughly vertical profiles. Measurements from distinct regions within one or more profiles are often averaged to reduce the uncertainty in the measurement. Here, we will calculate κ using the methods described in the previous section based on a limited number of 1D vertical profiles extracted from the simulations. Note that the profiles that we use are taken instantaneously and are perfectly vertical. How well this describes oceanographic measurements depends on the fall speed of the instrument and the speed of the currents. Some platforms such as microstructure gliders make significantly inclined profiles, although these data are often analyzed in a similar way to free-falling profilers (e.g. Palmer et al. (2015)).

We extract data from the simulations by randomly selecting a set of vertical profiles from a single three-dimensional field. Since the simulations were sampled when the flow is in a statistically stationary state, sampling at different spatial locations should give the same statistical result as sampling at different time intervals. Treating a limited number of samples as independent vertical profiles is justified by the horizontal de-correlation of statistical quantities. For example, the horizontal autocorrelation length associated with the profile-averaged TKE dissipation rate $\langle \varepsilon \rangle_z$

drops to zero at a distance of $L_z/2$ or 5 m in Simulation C and a distance of $\sim 2L_z$ or ~ 10 m in Simulations A and B. Note that the properties of the large-scale flow in the simulations will be influenced by the forcing scheme used. In the ocean, where turbulence is associated with eddies, internal waves, and shear layers across a wide range of horizontal scales, the de-correlation distance between profile-averaged statistics could be much larger than 10 m.

Before testing the methods for estimating κ it is useful to quantify the variability in profile-averaged statistics induced by intermittent stratified turbulence. Figure 5 shows the probability density function (PDF) of the buoyancy flux, TKE and potential energy dissipation rates, and squared Thorpe scale, each normalized by the corresponding volume average. Here the Thorpe scale is calculated by averaging the *rms* displacement over one vertical profile such that

$$L_T^z \equiv \left\langle L_d^2 \right\rangle_z^{1/2}. \tag{23}$$

Each PDF is calculated using the full 3D computational volume (i.e. vertical profiles were collected at every horizontal gridpoint). The Thorpe scale is squared for comparison with the other quantities since this quantity appears in the expression for κ_T.

The modes of the PDFs for all quantities shown in Figure 5 are skewed towards values smaller than the volume average. It is well known in the turbulence literature that the point-wise TKE and variance dissipation rates are similarly skewed such that a small number of large values contribute significantly to the volume average (Pope 2000). The PDFs of local (pointwise) ε and χ are typically assumed to be lognormal, following Kolmogorov (1962). de Bruyn Kops (2015) shows that distributions of local ε and χ in stratified turbulence are well-approximated by the lognormal model provided that $\mathrm{Re_b} > O(10)$. The TKE dissipation rate measured in the ocean thermocline is similarly skewed (Baker and Gibson 1987; Gregg et al. 1996). Evidently the intermittency inherent in the point-wise statistics extends to the profile-averaged statistics.

Here, we calculate ε and χ using derivatives of all three velocity components and buoyancy in all three spatial directions. Field measurements of these quantities generally involve a subset of the velocity and/or gradient information and assumptions about the isotropy of the small-scale turbulence are invoked to fill in the missing information. The PDFs of the surrogates for ε and χ based on a subset of the velocity and scalar gradients are significantly different from those of the exact quantities. In particular, the left side of the distributions of the surrogates tend toward exponential (Almalkie and de Bruyn Kops 2012a; de Bruyn Kops 2015) and the mean of the surrogates are significantly different from the exact values when $\mathrm{Re_b}$ is low (Hebert and de Bruyn Kops 2006b).

The variance associated with the buoyancy flux is much larger than the variance in other quantities. This appears to be associated with a large contribution from internal waves. Figure 2 shows regions with alternating sign of $w'b'$, indicating active exchange between kinetic and potential energy. The profile-averaged buoyancy flux is often negative (not shown in Figure 5). As we will see below, the large variability in the profile-averaged buoyancy flux has significant implications for the estimates of κ.

Based on simulations of Kelvin-Helmholtz (K-H) instability, Smyth et al. (2001) proposed that the ratio of the Ozmidov and Thorpe scales provides a measure of the 'age' of a turbulent event. Their simulations started with a laminar stratified shear layer that was unstable to K-H. During initial roll-up of the K-H billows, they found that the Thorpe scale grows quickly, but dissipation remains low and as a result $L_O/L_T << 1$. In the later stages of their simulations, three-dimensional turbulence develops, and $L_O \sim L_T$. In simulations at substantially higher Reynolds number, Mashayek et al. (2017a) found analogous behaviour, although they interpreted the (overall) monotonic increase in L_O/L_T during the turbulent life cycle as being due to the relatively slower decrease in L_O compared to L_T during the turbulent decay phase of the life cycle. Mater et al. (2015) apply a similar argument to explain variations in L_O/L_T in convectively-generated

turbulence. Observations reported in Smyth et al. (2001), Mater et al. (2015) and Mashayek et al. (2017a) all show relatively broad distributions of L_O/L_T.

Probability density functions of L_O^z/L_T^z (where the dissipation rate and Thorpe displacement are calculated based on averages over individual vertical profiles) is shown in Figure 6(a). The peak in the distribution for Simulation C is relatively close to the value of $L_O/L_T = 0.8$ proposed by Dillon and Caldwell (1980), and the distribution qualitatively resembles the observations reported in Smyth et al. (2001). The ratio of the Ozmidov to Thorpe scale is somewhat smaller in Simulations A and B. This is consistent with the observations reported in Mater et al. (2015) which suggest that L_O/L_T is not constant and depends on the properties of the flow. The spread in the distributions of L_O^z/L_T^z suggests that the collection of profile-averaged statistics can be viewed as an ensemble of turbulent events as visualized in Figure 1.

Figure 6(b) shows PDFs of mixing efficiency calculated using the profile-averaged dissipation rates, i.e. $\langle\chi\rangle_z/\left(\langle\chi\rangle_z+\langle\varepsilon\rangle_z\right)$, which exhibits significant scatter about the volume average. The mean and mode of the distributions increase from Simulation A to Simulation C as the buoyancy Reynolds number increases. The mean values are somewhat larger than the canonical value of 1/6, ranging from 0.18 in Simulation A to 0.28 in simulation C, although the spread about the mean is considerable. For example $\sim 22\%$ of the profiles taken from Simulation C have a mixing efficiency larger than 0.4, although such large values do arise in idealised flows subject to strong Kelvin-Helmoltz-like shear-driven overturning motions (see for example Mashayek et al. (2013, 2017a)).

Some recent studies have suggested that the mixing efficiency depends on the buoyancy Reynolds number, $Re_b \equiv \varepsilon/(\nu N^2)$ (e.g. Shih et al. (2005); Mater and Venayagamoorthy (2014); Salehipour et al. (2016); Mashayek et al. (2017b); Monismith et al. (2018)). Although there are differences in the details of various proposed scalings, most of the observations and simulations

reported in these papers suggest a decrease in the mixing efficiency when Re_b exceeds a critical value. Figure 6(c) shows the mixing efficiency plotted against Re_b, with each quantity calculated from the profile-averaged dissipation rates. For small Re_b the mixing efficiency is very close to the value of 0.17 proposed by Osborn (1980), and consistent with previous numerical simulations (e.g. Shih et al. (2005)). A peak in mixing efficiency for moderate values of Re_b as seen in Figure 6(c) also occurs in some of the simulations from Shih et al. (2005) (see also Mater and Venayagamoorthy (2014) and Salehipour and Peltier (2015)). Here, the mixing efficiency decreases with increasing buoyancy Reynolds number for $Re_b \gtrsim 800$. This value is significantly larger than the threshold value found by Shih et al. (2005), but smaller than the value from observations reported in Lozovatsky and Fernando (2013) and well within the range of other simulations and observations (Mater and Venayagamoorthy 2014; Monismith et al. 2018).

Estimates of the vertical diffusivity calculated using sets of randomly selected vertical profiles are shown in Figure 7. Specifically, when applied to n vertical profiles, the vertical diffusivity estimated from the Osborn-Cox, Osborn, and Thorpe methods can be written

$$\kappa_{O-C}^{z,n} = \frac{\langle \chi \rangle_{z,n}}{\langle N^2 \rangle_{z,n}}, \quad \kappa_O^{z,n} = \Gamma \frac{\langle \varepsilon \rangle_{z,n}}{\langle N^2 \rangle_{z,n}}, \quad \kappa_T^{z,n} = 0.64\Gamma \left(\langle L_T^z \rangle_n \right)^2 \langle N^2 \rangle_{z,n}^{1/2}, \tag{24}$$

respectively, where $\langle \cdot \rangle_{z,n}$ denotes an average over n vertical profiles and L_T^z is defined in Eq. (23). Similarly, the vertical diffusivity associated with the direct method applied to n vertical profiles is

$$\kappa_d^{z,n} = \frac{-\langle B \rangle_{z,n}}{\langle N^2 \rangle_{z,n}}. \tag{25}$$

Note that here $\langle N^2 \rangle_{z,n} = N_0^2$ due to the periodicity of the computational domain. In Figure 7 each estimate of κ is dimensionalized such that the height of the vertical domain and the length of each profile is 5 m. Solid colored lines show ± 1 standard deviation about the mean and the area between these curves is shaded to highlight the uncertainty associated with each estimate. Black

dashed lines indicate the vertical diffusivity calculated with the volume-averaged buoyancy flux, i.e. κ_d^V.

In all cases, $\kappa_d^{z,n}$ converges very slowly to κ_d^V. Figure 8 shows the standard deviation of the averages of the buoyancy flux, kinetic and potential energy dissipation rates, and the squared Thorpe scale for a given number of vertical profiles. In all cases the standard deviation decreases with the square root of the number of profiles (compare with dashed line) as expected from the central limit theorem for independent random variables. However, even with 20 profiles, negative values of $\kappa_d^{z,n}$ are within one standard deviation of the mean in Simulations A and B. The variance is smaller in Simulation C where the flow is more turbulent.

The standard deviations associated with the profile-averaged dissipation rate and Thorpe scales are much smaller than the standard deviation of the buoyancy flux in Simulations A and B. As seen in Figure 4, the Osborn and Osborn-Cox methods give a relatively good estimate of κ_d^V in these cases. Interestingly, the standard deviations of $\langle \varepsilon \rangle_{z,n}$ and $\langle \chi \rangle_{z,n}$ are significantly larger in Simulation C and as a result the Osborn and Osborn-Cox methods require more profiles to converge in this case. Since Simulation C is the most turbulent, having the largest dissipation rate, diffusivity, and buoyancy Reynolds number, the slow convergence of the Osborn and Osborn-Cox methods is unexpected and an explanation for this behavior is not immediately clear. In comparison, the Thorpe-scale method converges relatively quickly in Simulation C.

e. Validity of assumptions underlying the Osborn and Osborn-Cox methods

Remarkably, when applied to a limited number of vertical profiles, the Osborn and Osborn-Cox relations (Equations 17 and 13) outperform their underlying assumptions. Figure 9 shows the normalized residual associated with the classic Osborn relation (Eq. 17, solid blue curve) and the classic Osborn-Cox relation (Eq. 13, dashed blue curve). Here, the normalized residual is defined

as the absolute value of the sum of the terms in each relation (with all terms on one side of the relevant equation) divided by the sum of the absolute values of each individual term.

For the Osborn model, we also evaluate the assumption that the turbulent flux coefficient Γ is constant (solid green curve), and the assumed quasi-steady balance (unaffected by advection) in the TKE budget (Eq. 14, solid red curve). The vertical and profile average is not shown in the legend for notational clarity but is applied to ε, B, P, and N^2 individually. We also evaluate the assumption underlying the Osborn-Cox model that the buoyancy variance budget reduces to a production/dissipation balance with $B \simeq \chi$ (dashed red curve).

One might expect the error associated with the Osborn and Osborn-Cox relations to be at least as large as that of the worst assumption underlying these relations. Instead, the error associated with the Osborn relation is significantly less than the errors associated with the equations for the flux coefficient and TKE budgets for Simulations A and B. In case C the error in the Osborn relation is comparable to the error associated with the flux coefficient and smaller than the error associated with the TKE budget. A similar conclusion applies to the Osborn-Cox model where the Osborn-Cox relation (dashed blue curve in Fig. 9) significantly outperforms the assumption of production/dissipation balance in the buoyancy variance equation (dashed red curve) in Simulations A and B.

An important difference between the Osborn and Osborn-Cox relations and the equations for the flux coefficient and the TKE and buoyancy variance budgets underlying these relations is that the buoyancy flux does not appear explicitly in the Osborn or Osborn-Cox relations. Figure 7 showed that the buoyancy flux exhibits very large scatter about its mean value, and this is particularly true in Simulations A and B. One explanation for the relatively low normalized residuals associated with the Osborn and Osborn-Cox relations is they are it is not influenced by the reversible contributions of internal waves to the buoyancy flux. Indeed, central to the averaging at the heart of the

Osborn method is the assumption that reversible processes in the buoyancy flux are filtered out, leaving only the irreversible component, capturing the actual mixing occuring within the flow.

Relatively recently, Salehipour and Peltier (2015) proposed a 'generalized Osborn relation' using the framework introduced by Winters and D'Asaro (1996), designed explicitly to identify, as a function of time, the diapycnal diffusivity in terms of an appropriate definition for an inherently irreversible mixing efficiency. They showed that the diapycnal diffusivity κ_ρ can be written as

$$\kappa_\rho = \frac{\mathscr{E}}{1-\mathscr{E}} \frac{\varepsilon}{N_*^2}, \tag{26}$$

where $\mathscr{E}$ is the *irreversible* and instantaneous mixing efficiency defined in Caulfield and Peltier (2000) and N_* is the buoyancy frequency calculated using the sorted density profile. Since this expression relies on quantities calculated from (volume) sorted data, it is a global measure of the mixing within the entire domain under consideration, but can in principle be calculated at every time instant within a temporally evolving flow. As the key parameters (such as an appropriately defined buoyancy Reynolds number and Richardson number) describing their simulated flow also vary in time, the results of their simulations, showing temporal variation of $\mathscr{E}$ can be interpreted as evidence that $\mathscr{E}$ depends on such parameters (Salehipour and Peltier 2015; Salehipour et al. 2016). Importantly, Eq. (26) does not rely on any assumptions aside from the Boussinesq approximation.

Salehipour and Peltier (2015) noted the clear structural similarity between Eq. (26) and the Osborn relation, Eq. (17). For strongly stratified flows with relatively small isopycnal displacements one might anticipate that the globally sorted buoyancy frequency $N_* \simeq N$. To the extent that the flux coefficient Γ in Eq. (17) approximates the irreversible flux coefficient $\mathscr{E}/(1-\mathscr{E})$, the Osborn relation could then provide a relatively robust approximation to the diapycnal diffusivity. Fundamentally, the key point is that assuming that the *irreversible* buoyancy flux is some fraction of the turbulent dissipation rate appears to be a reasonable assumption.

The dissipation rates of turbulent kinetic energy (ε) and perturbation potential energy (χ) both represent irreversible losses from turbulence. As noted above, the partitioning of the total energy lost between these two terms is broadly consistent with the value of the flux coefficient used in the Osborn method, even though the theoretical arguments and assumptions presented by Osborn to justify this partitioning are not satisfied, not least due to the contaminating effects of *reversible* processes. The apparently robust partitioning between perturbation kinetic and potential energy dissipation might help explain why the Osborn method, applied using a limited number of vertical profiles, appears to be less prone to errors introduced by the presence of internal waves and other reversible processes than the failure of its underlying assumptions might suggest. It should be kept in mind that this discussion pertains to averaged quantities and that in local, transient mixing events the relative size of ε and χ can vary substantially.

4. Conclusions and discussion

In this paper we tested the performance of the Osborn, Osborn-Cox, and Thorpe-scale methods using high resolution direct numerical simulations (DNS). The simulations used an idealized triply periodic computational domain with an imposed background stratification. Turbulence was forced using a deterministic body force added to the momentum equations. The simulations can be viewed as a model of turbulence in a small region embedded within the thermocline. Three simulations were run with varying stratification and turbulence levels, typical of conditions in the main and seasonal thermoclines.

When the Osborn and Osborn-Cox methods are applied to the volume-averaged TKE and perturbation potential energy dissipation rate, the resulting estimates of the vertical turbulent diffusivity (κ_O^V and κ_{O-C}^V) are within 40% of the value obtained directly from the volume-averaged turbulent buoyancy flux, κ_d^V. When the Thorpe scale is calculated using individual vertical profiles and then

averaged over the full computational domain, the resulting estimate, κ_T^V is very close to κ_O^V in Simulation C but significantly overestimates κ_d^V in Simulations A and B with relatively small Re_b. In Simulation A, κ_T^V is more than 2.5 times larger than κ_d^V.

Consistent with previous simulations of forced stratified turbulence, we find that turbulence is inherently patchy and intermittent. For example, the PDFs of the dissipation rates of kinetic energy and buoyancy variance are skewed with a small number of very intense events, associated with vigorous, shear-driven overturnings. We find that this intermittency extends to the statistics averaged over one-dimensional vertical profiles, despite the fact that the simulations are set up such that each profile has the same average stratification.

This finding has important implications for the interpretation of limited observational datasets and for sampling strategies. For example, to ensure that the average dissipation rate can be correctly calculated, it would be necessary to ensure that enough of the extreme events are captured. The rate at which the various estimates of κ converge to the values calculated with volume-averaged statistics depends on Re_b. In general, the Osborn and Osborn-Cox methods converge relatively quickly in the simulations with small values of Re_b, while the Thorpe-scale method converges somewhat faster in Simulation C at larger Re_b than in Simulations A and B.

In comparison to the Osborn and Osborn-Cox methods, the diffusivity calculated directly from the vertical buoyancy flux using a small number of vertical profiles exhibits a very large scatter about the mean. Remarkably in Simulations A and B, negative values of κ are within one standard deviation of the average even when using 20 vertical profiles, each 5m in length. The convergence to the mean is faster in Simulation C where the flow is more turbulent. The slow convergence of the buoyancy flux for small Re_b appears to be due to large (and inherently reversible) contributions from internal waves. In an internal wave field the sign of $w'b'$ fluctuates as energy is transferred between the kinetic energy reservoir and the potential energy reservoir. A large averaging window

(in space, in time or in ensemble) is required to eliminate these reversible contributions to the buoyancy flux.

Here, we have not tested the performance of finescale methods which rely on measurements of internal waves. The large-scale forcing that was used to drive turbulence in the DNS was idealized and was not necessarily intended to replicate the properties of the finescale internal wave field. Simulations that simultaneously resolve a typical finescale internal wave spectrum (e.g. Gargett et al. (1981)) while also resolving small-scale turbulence and mixing could be used to test (and perhaps improve) finescale methods.

Acknowledgements

The authors would like to thank the Editor, Jim Moum, Matthew Alford, and an anonymous referee for constructive comments. We acknowledge the support of EPSRC under the Programme Grant EP/K034529/1 'Mathematical Underpinnings of Stratified Turbulence' (MUST), and from the European Research Council (ERC) under the European Union's Horizon 2020 research and innovation Grant No 742480 'Stratified Turbulence And Mixing Processes' (STAMP), and also support from the U.S. Office of Naval Research under grant N00014-15-1-2248. High performance computing resources were provided through the U.S. Department of Defense High Performance Computing Modernization Program by the Army Engineer Research and Development Center and the Army Research Laboratory under Frontier Project FP-CFD-FY14-007.

References

Alford, M., and R. Pinkel, 2000a: Patterns of turbulent and double-diffusive phenomena: Observations from a rapid-profiling microconductivity probe. *J. Phys. Oceanogr.*, **30**, 833–854.

Alford, M. H., and R. Pinkel, 2000b: Observations of overturning in the thermocline: The context of ocean mixing. *J. Phys. Oceanogr.*, **30**, 805–832.

Almalkie, S., and S. M. de Bruyn Kops, 2012a: Energy dissipation rate surrogates in incompressible Navier-Stokes turbulence. *J. Fluid Mech.*, **697**, 204–236.

Almalkie, S., and S. M. de Bruyn Kops, 2012b: Kinetic energy dynamics in forced, homogeneous, and axisymmetric stably stratified turbulence. *J. Turbul.*, **13 (29)**, 1–29.

Baker, M. A., and C. H. Gibson, 1987: Sampling turbulence in the stratified ocean: Statistical consequences of strong intermittency. *Journal of Physical Oceanography*, **17 (10)**, 1817–1836.

Caulfield, C. P., and W. R. Peltier, 2000: The anatomy of the mixing transition in homogeneous and stratified free shear layers. *J. Fluid Mech.*, **413**, 1–47.

Comte-Bellot, G., and S. Corrsin, 1971: Simple Eulerian time correlation of full and narrow-band velocity signals in grid-generated 'isotropic' turbulence. *J. Fluid Mech.*, **48**, 273–337.

de Bruyn Kops, S. M., 2015: Classical turbulence scaling and intermittency in stably stratified Boussinesq turbulence. *J. Fluid Mech.*, **775**, 436–463.

de Bruyn Kops, S. M., and J. J. Riley, 2019: The effects of stable stratification on the decay of initially isotropic homogeneous turbulence. *J. Fluid Mech.*, **860**, 787821, doi:10.1017/jfm.2018.888.

Dillon, T. M., and D. R. Caldwell, 1980: The Batchelor spectrum and dissipation in the upper ocean. *J. Geophysical Research*, **85 (C4)**, 1910–1916.

Ferron, B., H. Mercier, K. Speer, A. Gargett, and K. Polzin, 1998: Mixing in the Romanche fracture zone. *Journal of Physical Oceanography*, **28 (10)**, 1929–1945.

Gargett, A., and T. Garner, 2008: Determining Thorpe scales from ship-lowered CTD density profiles. *Journal of Atmospheric and Oceanic Technology*, **25 (9)**, 1657–1670.

Gargett, A., P. Hendricks, T. Sanford, T. Osborn, and A. Williams, 1981: A composite spectrum of vertical shear in the upper ocean. *Journal of Physical Oceanography*, **11 (9)**, 1258–1271.

Gibson, C. H., 1980: Fossil turbulence, salinity, and vorticity turbulence in the ocean. *Marine Turbulence*, J. C. Nihous, Ed., Elsevier, 221–257.

Gregg, M., 1989a: Scaling turbulent dissipation in the thermocline. *Journal of Geophysical Research: Oceans*, **94 (C7)**, 9686–9698.

Gregg, M., 1999: Uncertainties and limitations in measuring ε and χ_t. *Journal of Atmospheric and Oceanic Technology*, **16 (11)**, 1483–1490.

Gregg, M., E. D'Asaro, J. Riley, and E. Kunze, 2018: Mixing efficiency in the ocean. *Annual review of marine science*, **10**, 443–473.

Gregg, M., D. Winkel, T. Sanford, and H. Peters, 1996: Turbulence produced by internal waves in the oceanic thermocline at mid and low latitudes. *Dynamics of atmospheres and oceans*, **24 (1-4)**, 1–14.

Gregg, M. C., 1989b: Scaling turbulent dissipation in the thermocline. *J. Geophys. Res.*, **94**, 9686–9698.

Hebert, D. A., and S. M. de Bruyn Kops, 2006a: Predicting turbulence in flows with strong stable stratification. *Phys. Fluids*, **18 (6)**, 1–10.

Hebert, D. A., and S. M. de Bruyn Kops, 2006b: Relationship between vertical shear rate and kinetic energy dissipation rate in stably stratified flows. *Geophys. Res. Let.*, **33**, L06 602, doi: doi:10.1029/2005GL025071.

Henyey, F. S., J. Wright, and S. M. Flatté, 1986: Energy and action flow through the internal wave field: An eikonal approach. *Journal of Geophysical Research: Oceans*, **91 (C7)**, 8487–8495.

Ivey, G. N., and J. Imberger, 1991: On the nature of turbulence in a stratified fluid. Part 1: The energetics of mixing. *J. Phys. Oceanogr.*, **21**, 650–658.

Johnson, H. L., and C. Garrett, 2004: Effects of noise on Thorpe scales and run lengths. *Journal of physical oceanography*, **34 (11)**, 2359–2372.

Kolmogorov, A. N., 1962: A refinement of previous hypotheses concerning the local structure of turbulence in a viscous incompressible fluid at high Reynolds number. *J. Fluid Mech.*, **13**, 82–85.

Large, W. G., J. C. McWilliams, and S. C. Doney, 1994: Oceanic vertical mixing - a review and a model with a nonlocal boundary-layer parameterization. *Rev. Geophys.*, **32**, 363–403.

Lindborg, E., 2006: The energy cascade in a strongly stratified fluid. *J. Fluid Mech.*, **550**, 207–242.

Lozovatsky, I. D., and H. J. S. Fernando, 2013: Mixing efficiency in natural flows. *Philosophical Transactions of the Royal Society of London A: Mathematical, Physical and Engineering Sciences*, **371 (1982)**, 20120 213.

MacKinnon, J., and M. Gregg, 2003: Mixing on the late-summer New England shelf – solibores, shear, and stratification. *Journal of Physical Oceanography*, **33 (7)**, 1476–1492.

747 Maffioli, A., and P. A. Davidson, 2016: Dynamics of stratified turbulence decaying from a high
748 buoyancy Reynolds number. *J. Fluid Mech.*, **786**, 210–233.

749 Marra, J., R. Bidigare, and T. Dickey, 1990: Nutrients and mixing, chlorophyll and phytoplankton
750 growth. *Deep Sea Research Part A. Oceanographic Research Papers*, **37 (1)**, 127–143.

751 Marshall, J., and K. Speer, 2012: Closure of the meridional overturning circulation through south-
752 ern ocean upwelling. *Nature Geoscience*, **5 (3)**, 171.

753 Mashayek, A., C. P. Caulfield, and W. R. Peltier, 2013: Time-dependent, non-monotonic mixing
754 in stratified turbulent shear flows: implications for oceanographic estimates of buoyancy flux. *J.*
755 *Fluid Mech.*, **736**, 570–593.

756 Mashayek, A., C. P. Caulfield, and W. R. Peltier, 2017a: Role of overturns in optimal mixing in
757 stratified mixing layers. *J. Fluid Mech.*, **826**, 522–552.

758 Mashayek, A., H. Salehipour, D. Bouffard, C. P. Caulfield, R. Ferrari, M. Nikurashin, W. R.
759 Peltier, and W. D. Smyth, 2017b: Efficiency of turbulent mixing in the abyssal ocean circulation.
760 *Geophys. Res. Lett.*, **44**, 6296–6306.

761 Mater, B. D., and S. K. Venayagamoorthy, 2014: A unifying framework for parameterizing stably
762 stratified shear-flow turbulence. *Phys. Fluids*, **26 (3)**, doi:{10.1063/1.4868142}.

763 Mater, B. D., S. K. Venayagamoorthy, L. St. Laurent, and J. N. Moum, 2015: Biases in Thorpe-
764 scale estimates of turbulence dissipation. Part I: Assessments from large-scale overturns in
765 oceanographic data. *Journal of Physical Oceanography*, **45 (10)**, 2497–2521.

766 Monismith, S. G., J. R. Koseff, and B. L. White, 2018: Mixing efficiency in the presence of
767 stratification: when is it constant? *Geophys. Res. Lett.*, **45**, 5627–5634.

Moum, J., M. Gregg, R. Lien, and M. Carr, 1995: Comparison of turbulence kinetic energy dissipation rate estimates from two ocean microstructure profilers. *Journal of Atmospheric and Oceanic Technology*, **12 (2)**, 346–366.

Moum, J. N., 1996: Energy-containing scales of turbulence in the ocean thermocline. *J. Geophys. Res.-Oceans*, **101**, 14 095–14 109.

Osborn, T. R., 1980: Estimates of the local-rate of vertical diffusion from dissipation measurements. *J. Phys. Oceanogr.*, **10**, 83–89.

Osborn, T. R., and C. S. Cox, 1972: Oceanic fine structure. *Geophysical & Astrophysical Fluid Dynamics*, **3 (1)**, 321–345.

Overholt, M. R., and S. B. Pope, 1998: A deterministic forcing scheme for direct numerical simulations of turbulence. *Computers & Fluids*, **27**, 11–28.

Pacanowski, R., and S. Philander, 1981: Parameterization of vertical mixing in numerical models of tropical oceans. *Journal of Physical Oceanography*, **11 (11)**, 1443–1451.

Palmer, M., G. Stephenson, M. Inall, C. Balfour, A. Düsterhus, and J. Green, 2015: Turbulence and mixing by internal waves in the Celtic Sea determined from ocean glider microstructure measurements. *Journal of Marine Systems*, **144**, 57–69.

Polzin, K. L., J. M. Toole, and R. W. Schmitt, 1995: Finescale parameterizations of turbulent dissipation. *Journal of physical oceanography*, **25 (3)**, 306–328.

Pope, S. B., 2000: *Turbulent Flows*. Cambridge University Press, Cambridge.

Portwood, G. D., S. M. de Bruyn Kops, J. R. Taylor, H. Salehipour, and C. P. Caulfield, 2016: Robust identification of dynamically distinct regions in stratified turbulence. *J. Fluid Mech.*, **807**, R2 (14 pages).

Rao, K. J., and S. M. de Bruyn Kops, 2011: A mathematical framework for forcing turbulence applied to horizontally homogeneous stratified flow. *Phys. Fluids*, **23**, 065 110, doi:doi:10.1063/1.3599704.

Riley, J. J., and S. M. de Bruyn Kops, 2003: Dynamics of turbulence strongly influenced by buoyancy. *Phys. of Fluids*, **15 (7)**, 2047–2059.

Rorai, C., P. D. Mininni, and A. Pouquet, 2014: Turbulence comes in bursts in stably stratified flows. *Physical Review E*, **89 (4)**, 043 002.

Salehipour, H., and W. Peltier, 2015: Diapycnal diffusivity, turbulent Prandtl number and mixing efficiency in Boussinesq stratified turbulence. *J. Fluid Mech.*, **775**, 464–500.

Salehipour, H., W. R. Peltier, C. B. Whalen, and J. A. MacKinnon, 2016: A new characterization of the turbulent diapycnal diffusivities of mass and momentum in the ocean. *Geophys. Res. Lett.*, **43 (7)**, 3370–3379.

Scotti, A., 2015: Biases in Thorpe-scale estimates of turbulence dissipation. Part II: energetics arguments and turbulence simulations. *Journal of Physical Oceanography*, **45 (10)**, 2522–2543.

Shih, L. H., J. R. Koseff, G. N. Ivey, and J. H. Ferziger, 2005: Parameterization of turbulent fluxes and scales using homogeneous sheared stably stratified turbulence simulations. *J. Fluid Mech.*, **525**, 193–214.

Smyth, W. D., and J. N. Moum, 2000: Length scales of turbulence in stably stratified mixing layers. *Phys. Fluids*, **12**, 1327–1342.

Smyth, W. D., J. N. Moum, and D. R. Caldwell, 2001: The efficiency of mixing in turbulent patches: inferences from direct simulations and microstructure observations. *J. Phys. Oceanogr.*, **31**, 1969–1992.

Sreenivasan, K. R., 1998: An update on the energy dissipation rate in isotropic turbulence. *Phys. Fluids*, **10 (2)**, 528–529.

Sreenivasan, K. R., and R. A. Antonia, 1997: The phenomenology of small-scale turbulence. *Annu. Rev. Fluid Mech.*, **29**, 435–472.

Thorpe, S., 2005: The turbulent ocean, 439 pp. *Cambridge University*.

Thorpe, S. A., 1977: Turbulence and mixing in a Scottish loch. *Philos. Trans. Roy. Soc. London*, **A286**, 125–181.

Waite, M. L., 2011: Stratified turbulence at the buoyancy scale. *Phys. Fluids*, **23 (6)**, 066 602, doi:10.1063/1.3599699.

Wang, L. P., S. Y. Chen, J. G. Brasseur, and J. C. Wyngaard, 1996: Examination of hypotheses in the Kolmogorov refined turbulence theory through high-resolution simulations. Part 1. Velocity field. *J. Fluid Mech.*, **309**, 113–156.

Warhaft, Z., 2000: Passive scalar in turbulent flows. *Annu. Rev. Fluid Mech.*, **32**, 203–240.

Waterhouse, A. F., and Coauthors, 2014: Global patterns of diapycnal mixing from measurements of the turbulent dissipation rate. *Journal of Physical Oceanography*, **44 (7)**, 1854–1872.

Winters, K. B., and E. A. D'Asaro, 1996: Diascalar flux and the rate of fluid mixing. *Journal of Fluid Mechanics*, **317**, 179–193.

Wunsch, C., and R. Ferrari, 2004: Vertical mixing, energy, and the general circulation of the oceans. *Annu. Rev. Fluid Mech.*, **36**, 281–314.

LIST OF TABLES

Label	$\widetilde{L}_{x,y}$	$\widetilde{L}_z$	$N_{x,y}$	N_z	Re	Fr	Pr	$\mathrm{Fr_h}$	$\mathrm{Fr_t}$	$\mathrm{Re_h}$	$\mathrm{Re_t}$	Re_b
A	2π	$\pi/4$	9216	1152	6452	0.0416	7	0.071	0.0019	7048	82755	12.1
B	2π	$\pi/4$	18432	2304	2410	0.0416	7	0.080	0.0025	23069	231575	57.5
C	2π	π	13104	6552	4679	0.1667	7	0.45	0.015	2985	25597	241.5

TABLE 1. Nondimensional simulation parameters and derived quantities.

Label	$L_{x,y}$	L_z	$\Delta_{x,y,z}$	N_0^2	$\langle\varepsilon\rangle_V$	L_O^V	L_K^V	κ_d^V
A	40m	5m	4.3mm	$1.41\times10^{-5}\mathrm{s}^{-2}$	$1.71\times10^{-10}\mathrm{m}^2\mathrm{s}^{-3}$	5.6cm	8.7mm	$2.2\times10^{-6}\mathrm{m}^2\mathrm{s}^{-1}$
B	40m	5m	2.2mm	$2.00\times10^{-4}\mathrm{s}^{-2}$	$1.15\times10^{-8}\mathrm{m}^2\mathrm{s}^{-3}$	6.3cm	3.0mm	$1.8\times10^{-5}\mathrm{m}^2\mathrm{s}^{-1}$
C	10m	5m	0.76mm	$1.23\times10^{-4}\mathrm{s}^{-2}$	$2.97\times10^{-8}\mathrm{m}^2\mathrm{s}^{-3}$	14.8cm	2.4mm	$7.2\times10^{-5}\mathrm{m}^2\mathrm{s}^{-1}$

TABLE 2. Dimensional simulation parameters and derived quantities. The values here have been made dimensional by setting the vertical domain height $L_z = 5\mathrm{m}$ and kinematic viscosity $\nu = 10^{-6}\ \mathrm{m}^2\mathrm{s}^{-1}$ in each simulation.

LIST OF FIGURES

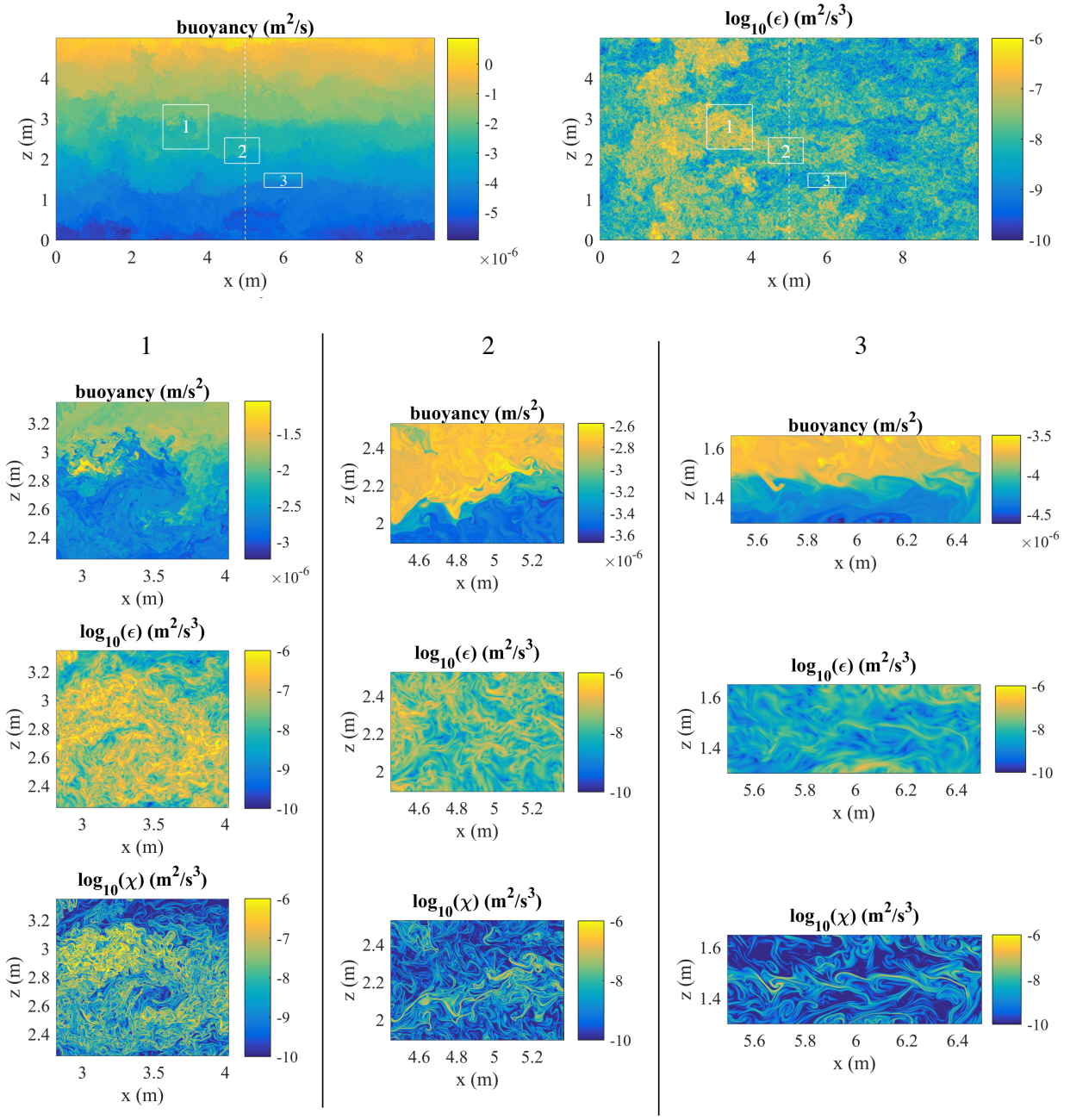

FIG. 1. Top row: dimensional buoyancy and turbulent kinetic energy dissipation rate (ε) on a vertical 2D slice extracted from Simulation C. Panels in columns 1, 2, and 3 show a close-up of regions with strong, moderate, and weak dissipation as indicated by the boxed regions labeled in the top row. The dissipation rate of perturbation potential energy (χ) is also shown. The white dashed lines in the top row indicate the location of the profile shown in Figure 2

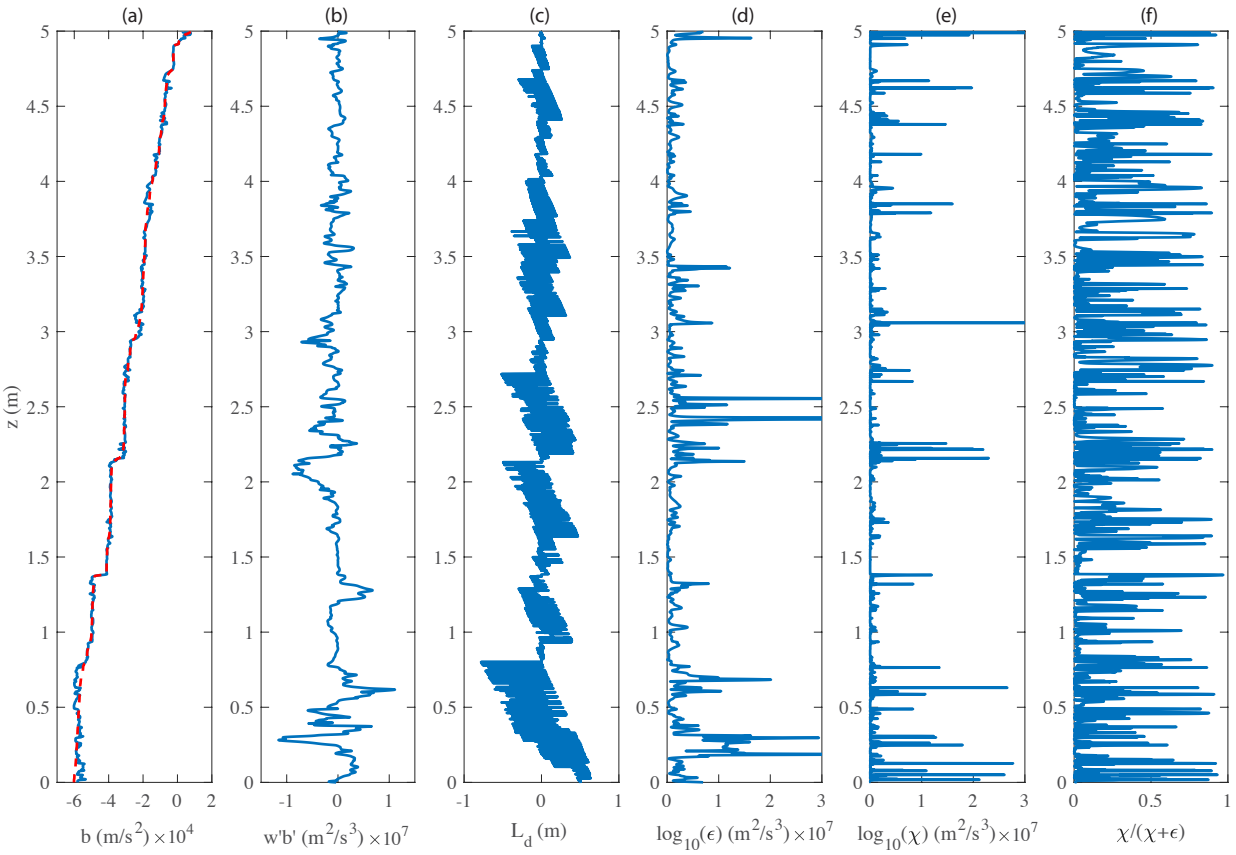

FIG. 2. Vertical profiles of (a) buoyancy, (b) buoyancy flux, (c) displacement scale L_d, (d) turbulent kinetic energy dissipation rate, (e) turbulent potential energy dissipation rate, and (f) local mixing efficiency extracted from Simulation C. The profiles are taken from the location indicated with a white dashed line in Figure 1. The dashed red line in (a) is the sorted density profile.

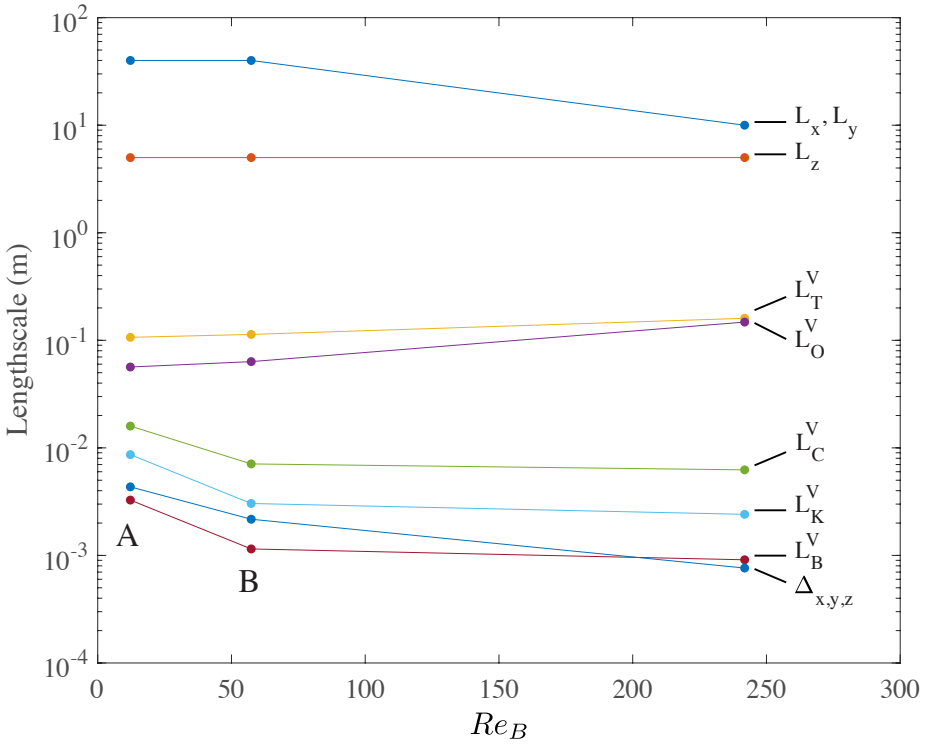

FIG. 3. Dimensional lengthscales: horizontal domain size L_x, L_y, vertical domain size L_z, Thorpe scale L_T^V, Ozmidov scale L_O^V, Kolmogorov scale L_K^V, Batchelor scale L_B^V, and grid spacing $\Delta_{x,y,z}$. Simulation labels are given at the bottom of each series. The volume-averaged dissipation rate was used to calculate L_O^V, L_K^V, and L_B^V, and the Thorpe scale was calculated by sorting individual 1D density profiles and averaging the resulting Thorpe scale over all horizontal grid points.

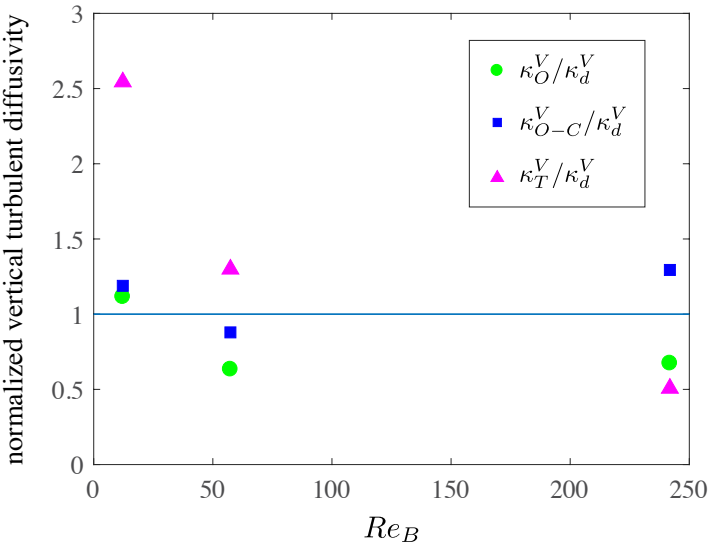

FIG. 4. Vertical diffusivity estimated using the Osborn method κ_O^V (green circles), Osborn-Cox method κ_{O-C}^V (blue squares), and Thorpe method κ_T^V (magenta triangles) , each calculated using data extracted from the full computational volume as defined in Eq. 22 and normalized by the turbulent vertical diffusivity diagnosed directly from the volume-averaged buoyancy flux, κ_d^V.

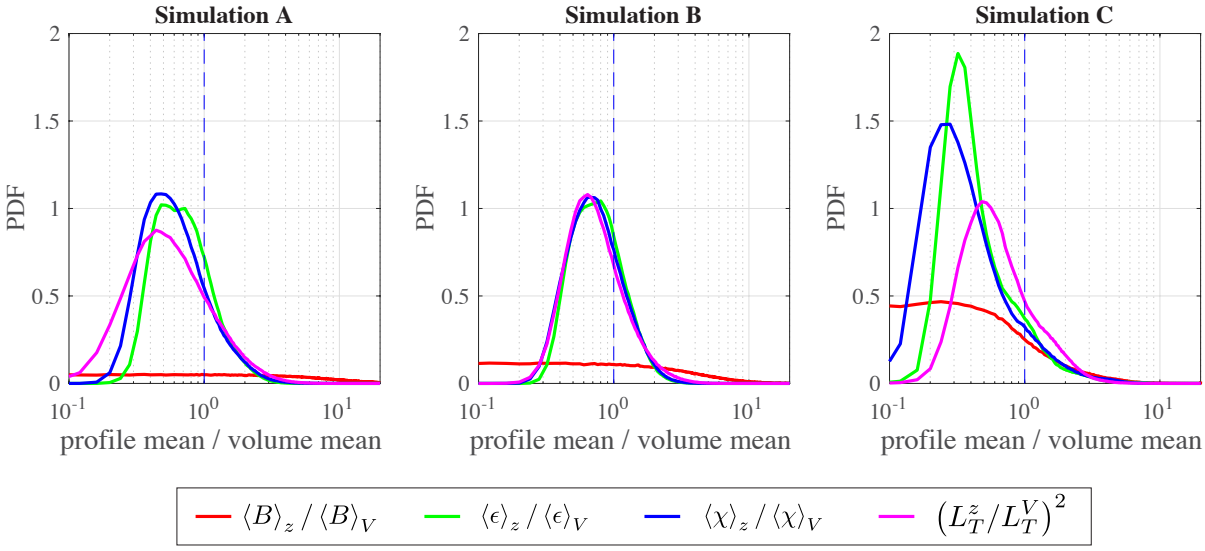

FIG. 5. PDFs of the profile-averaged buoyancy flux $\langle B\rangle_z$, kinetic energy dissipation rate $\langle \varepsilon\rangle_z$, potential energy dissipation rate $\langle \chi\rangle$, and Thorpe scale L_T^z, each normalized by the volume average. There are a significant number of profiles with $\langle B\rangle_z < 0$ which are not shown.

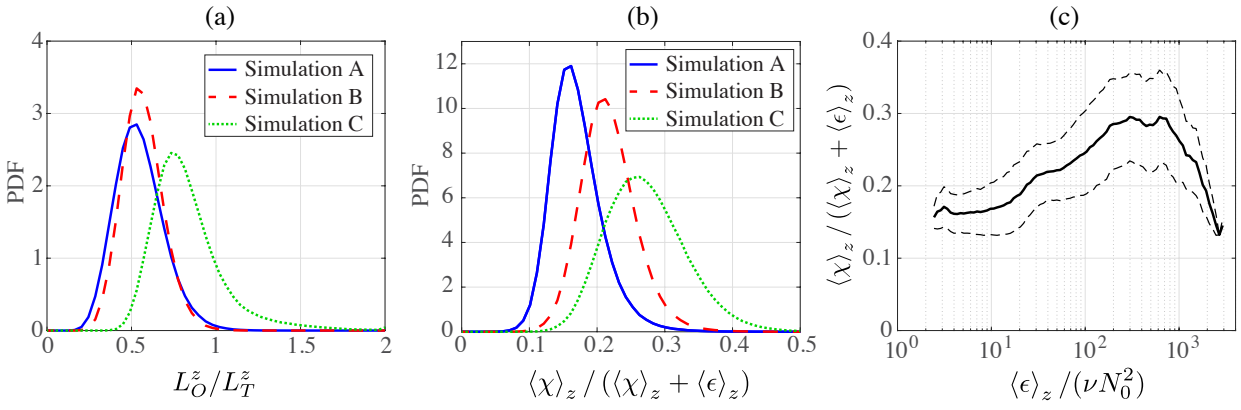

FIG. 6. Profile-averaged statistics: (a) Probability density function (PDF) associated with the ratio of the Ozmidov and Thorpe scales, (b) PDF of mixing efficiency, (c) mixing efficiency as a function of the buoyancy Reynolds number. Dashed lines in panel (c) indicate one standard deviation above and below the average value and averaging bins with fewer than 10 profiles are not shown.

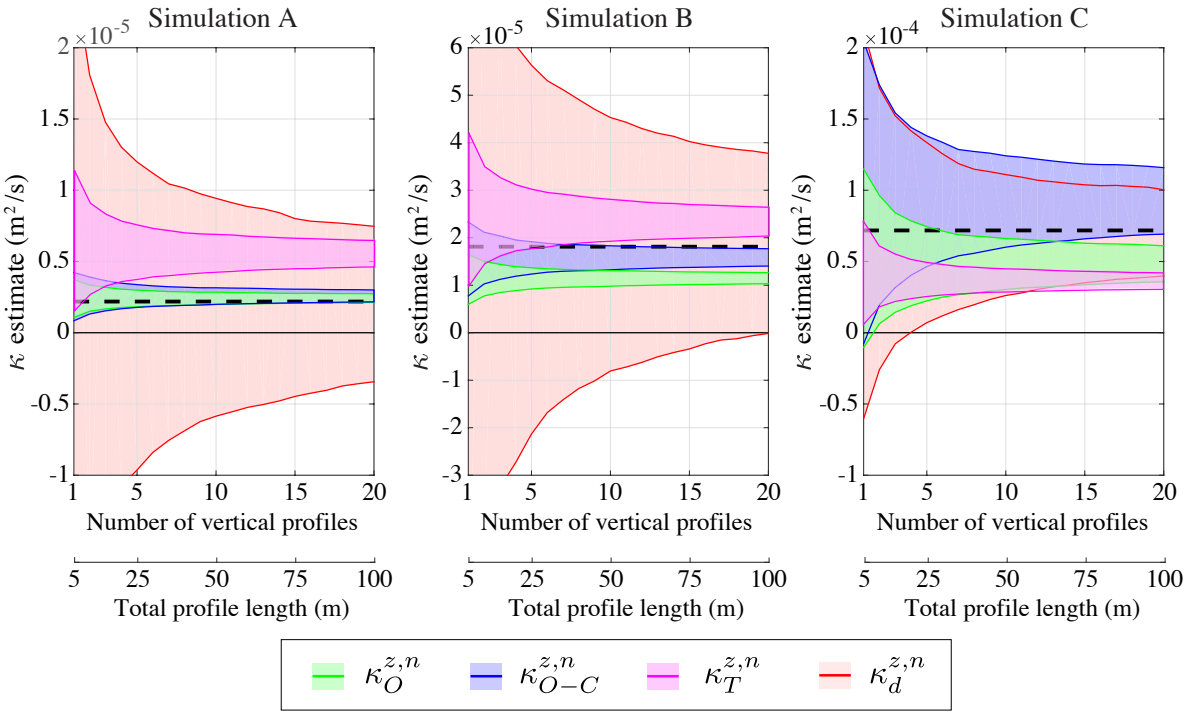

FIG. 7. Estimates of the vertical diffusivity using the Osborn (green), Osborn-Cox (blue), Thorpe (magenta), and direct methods (red), calculated using n vertical profiles. Lines denote ± 1 standard deviation about the mean and the area between these limits is shaded. The dashed line indicates the vertical diffusivity calculated by directly averaging the flux over the full volume of the simulations as defined in Eq. 21. Note that the limits of the vertical axis are different in each panel.

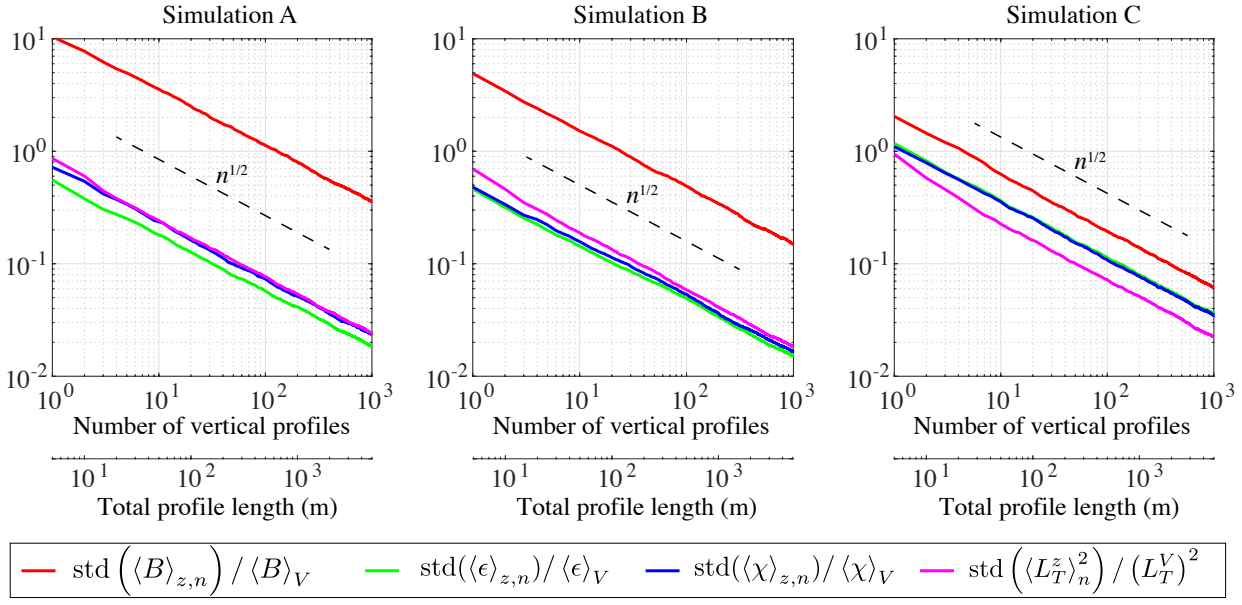

912 FIG. 8. Standard deviation associated with quantities averaged over n vertical profiles, normalized by the 3D
913 volume average. Dashed lines show the $n^{-1/2}$ scaling expected from the Central Limit Theorem.

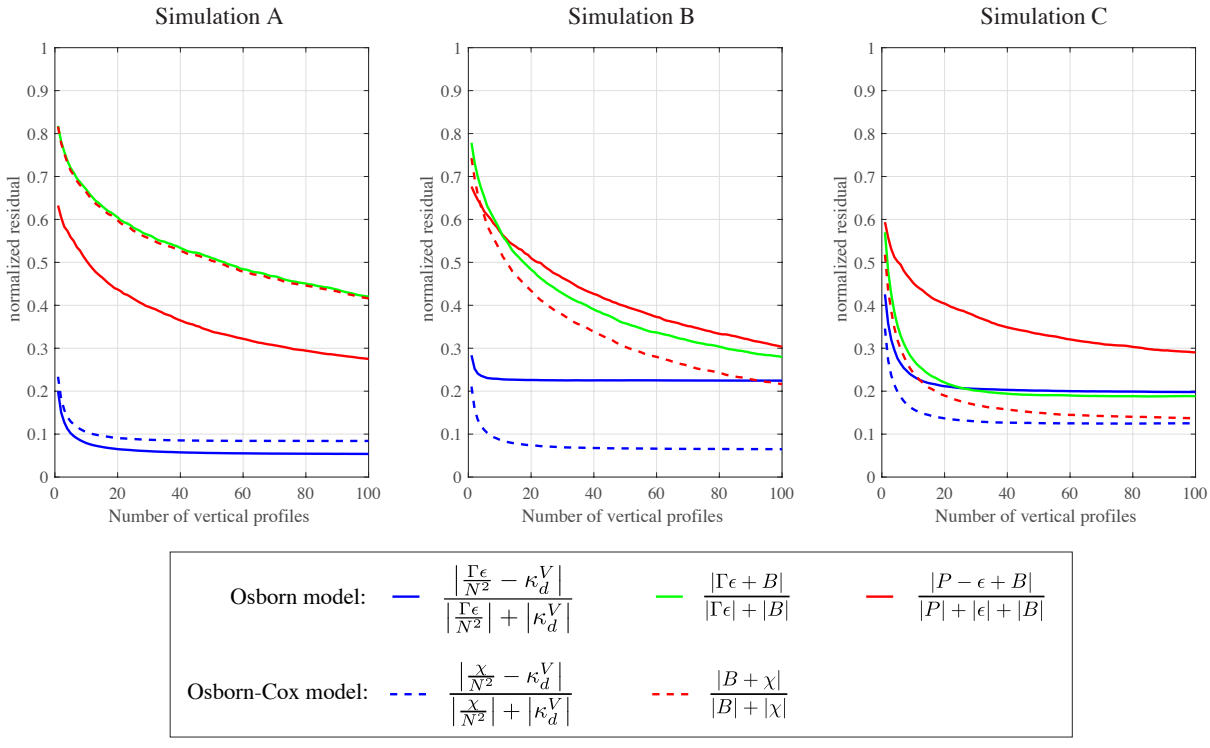

FIG. 9. Normalized residual associated with the Osborn and Osborn-Cox relations (blue) and several assumptions used to derive these relations (green and red). The values of ε, χ, B, P, and N^2 correspond to an average across the vertical domain and for the specified number of vertical profiles, e.g. $\langle\varepsilon\rangle_{z,n}$, and the averaging operators are omitted for clarity.